RESEARCH ARTICLE

In vitro 3D malignant melanoma model for the evaluation of hypericin-loaded oil-in-water microemulsion in photodynamic therapy

Hui L. Ma[1,2,3] · Wanlu Li[3] · Mian Wang[3] · Laudemir C. Varanda[1] · Janice R. Perussi[1] · Y. Shrike Zhang[3] · Emanuel Carrilho[1,2]

Abstract

Advances in biomimetic three-dimensional (3D) melanoma models have brought new prospects of drug screening and disease modeling, since their physiological relevancy for recapitulating in vivo tumor architectures is more accurate than traditional two-dimensional (2D) cell culture. Gelatin methacryloyl (GelMA) is widely used as a tissue-engineered scaffold hydrogel for 3D cell culture. In the present study, an in vitro 3D malignant melanoma model based on GelMA was fabricated to evaluate the efficiency of hypericin (Hy)-loaded microemulsion (ME) in photodynamic therapy against melanoma. The ME was produced by the spontaneous emulsification method to enhance the bioavailability of Hy at tumor sites. Hy-loaded MEs were applied to a 3D malignant melanoma model made using 6% GelMA and the co-culture of B16F10 and Balb/c 3T3 cells, followed by crosslinking using violet light (403 nm). The observation revealed excellent cell viability and the presence of F-actin cytoskeleton network. Hy-loaded MEs exhibited higher phototoxicity and cell accumulation (about threefold) than free Hy, and the cells cultured in the 3D system displayed lower susceptibility (about 2.5-fold) than those in 2D culture. These findings indicate that the developed MEs are potential delivery carriers for Hy; furthermore, GelMA hydrogel-based modeling in polydimethylsiloxane (PDMS) molds is a user-friendly and cost-effective in vitro platform to investigate drug penetration and provide a basis for evaluating nanocarrier efficiency for skin cancer and other skin-related diseases.

Keywords Malignant melanoma · 3D cell culture · Hypericin · Microemulsion · Photodynamic therapy

Introduction

Malignant melanoma is the most aggressive skin cancer type with high mortality, which bears the notorious hallmarks of elevated multidrug resistance and metastasis potential [1]. It is derived from the abnormal transformation of melanocytes that produce uncontrolled melanin in the basal layer of the epidermis because of ultraviolet (UV) radiation exposure [2]. Melanoma can also occur in specific skin areas not exposed to UV light but constantly subjected to enormous mechanical stress, such as in the palmoplantar and fingernail beds [3]. Although surgical excision remains the most common treatment applied to reduce the progression and eliminate the tumor, patients commonly suffer from deep lesions and cosmetic disfigurement [4]. Multiple treatment options are increasingly needed for minimizing the adverse effects and mortality. Thus, chemotherapy, radiotherapy, photodynamic therapy (PDT), immunotherapy, and targeted therapy can be adopted depending on the tumor location, disease stage and genetic profile [5].

PDT is a light-assisted treatment option that uses the combination of photosensitizer, visible light and oxygen to generate reactive oxygen species (ROS), unleashing irreversible damage to tumor cells and tumor-associated vascularization [6]. This treatment modality has been widely

✉ Y. Shrike Zhang
  yszhang@research.bwh.harvard.edu

✉ Emanuel Carrilho
  emanuel@iqsc.usp.br

1   Instituto de Química de São Carlos, Universidade de São Paulo, USP, Av. Trabalhador São-carlense, São Carlos, SP 13566-590, Brazil

2   Instituto Nacional de Ciência e Tecnologia de Bioanalítica, INCTBio, Campinas, SP 13083-970, Brazil

3   Division of Engineering in Medicine, Department of Medicine, Brigham and Women's Hospital, Harvard Medical School, Cambridge, MA 02139, USA

used for superficial cancers, including skin cancer, head and neck cancer, breast cancer, and basal cell carcinoma, due to its minimal invasiveness and highly selective cytotoxicity [7–10]. Studies have reported on PDT as a promising adjuvant therapy for patients with stage III/IV cutaneous metastatic melanomas [11].

Hypericin (Hy), a photosensitizer known as a nutraceutical with intense photosensitive activity, is present in *Hypericum perforatum* (Saint John's wort) [12]. It has low solubility in aqueous media with a log P (octanol/water) value of 3.43 [13], which is a substantial limitation for clinical applications; therefore, it needs novel topical formulations. Hence, we selected microemulsion (ME) to enhance Hy solubility and cell uptake for malignant melanoma. ME is produced spontaneously from two immiscible liquids, usually water and oil, stabilized by surfactants and co-surfactants and defined as a thermodynamically stable isotropic phase. It is a transparent system with droplet sizes ranging from 10 to 100 nm [14]. This nanocarrier enables a high solubilization capacity for hydrophobic compounds and acts as an enhancer for their penetration into skin and tissue. Due to its nanometric size, it can efficiently transport poorly soluble drugs in an aqueous medium [15]. Because of these properties, MEs have allowed the development of drug delivery systems for oral, intravenous, topical, and transdermal administration [16–19].

To overcome the limitations of conventional two-dimensional (2D) in vitro assays, three-dimensional (3D) cell culture has emerged as an alternative to 2D and animal models in studies on the mechanisms underlying melanoma progression, overcoming ethical considerations and feasibility issues. However, it provides fundamental absorption data from human and animal tissues that are difficult to obtain by in vivo studies [20]. Recent advanced 3D in vitro approaches include spheroid cell culture and melanoma skin equivalents. The spheroid cell culture relies on cell aggregation to form 3D clusters; it generally requires a higher number of initial cells and faces the challenges of building structures with complicated and relatively large geometries without adequate support [21]. Melanoma skin equivalents consist of artificial skin rebuilt from isolated cell populations, providing a more physiologically relevant melanoma scenario; however, there are technical challenges due to the specialized training and constant monitoring required during the prolonged culture time of up to 21 days [22].

Hydrogels have been widely used to inoculate cell self-assembled living structures. An advanced 3D cell culture model was established using the gelatin methacryloyl (GelMA) hydrogel to mimic malignant melanoma. The GelMA hydrogel is derived from hydrolyzed collagen and contains biological motifs, namely Arg-Gly-Asp (RGD) binding sequences, which provide cell attachment sites, promote intercellular interactions, and assist with oxygen diffusion and nutrient delivery [23]. The GelMA pre-polymer solution is a photocurable biomaterial with tunable physical properties for creating cell-laden constructs [24, 25]. These microengineered tissues can be utilized as in vitro models for recapitulating the heterogeneity and complex intracellular interactions of solid tumors and enable a more accurate simulation of the tumor microenvironment and phenotypes to evaluate the efficacy of therapeutic drugs before their in vivo testing and clinical trials. Several studies have shown that 3D melanoma cell cultures promote growth factor expression that is correlated with disease progression, allowing for the better prediction of chemotherapeutic drug resistance and melanoma metastasis [26, 27].

In the present study, we fabricated an in vitro 3D malignant melanoma model using photocurable GelMA to encapsulate B16F10 and Balb/c 3T3 cells, resulting in a co-cultured construct, which was used for evaluating the efficiency of Hy-loaded MEs in PDT. The spontaneous emulsification method was employed to produce these nanoformulations, characterized by particle size, shape, and physicochemical properties. For the 3D in vitro model, cell viability, proliferation, cytoskeleton, mechanical properties, and the expression of hypoxia-inducible factor-1 alpha (HIF-1α) were analyzed to ensure tumor tissue formation. Furthermore, Hy penetration and the intracellular accumulation from MEs were investigated using confocal laser scanning microscopy (CLSM).

Materials and methods

Materials

Hypericin was obtained through chemical synthesis carried out by Prof. Dr. Anderson Orzari Ribeiro (Federal University of ABC, Brazil) according to a previously reported protocol [28]. Oleic acid, propylene glycol, Tween 20 (hydrophilic-lipophilic balance, HLB = 16.7), and phosphotungstic acid were purchased from Synth, Brazil. Medium-chain triglyceride (MCT) was obtained from Athletica Clinical, Brazil. Tween 80 (HLB = 15.0), bovine serum albumin (BSA), 3-(4,5-dimethyl-2-thiazolyl)-2,5-diphenyl-2-H-tetrazolium bromide (MTT), cell counting kit-8 (CCK-8), porcine skin gelatin, methacrylic anhydride (MA), lithium phenyl-2,4,6-trimethyl-benzoyl phosphinate (LAP), human HIF-1α enzyme-linked immunosorbent assay (ELISA) kit, and Dulbecco's modified eagle medium (DMEM) were acquired from Sigma-Aldrich, USA. Fetal bovine serum (FBS) was purchased from Cultilab, Brazil. Singlet oxygen sensor green (SOSG), phalloidin-fluorescein isothiocyanate (FITC), 4',6-diamidine-2'-phenylindole dihydrochloride (DAPI), Live/DeaD viability/cytotoxicity kit, CellTracker Red CMTPX and CellTracker Green CMFDA

were obtained from Invitrogen, USA. Phosal® 50 PG (50% phosphatidylcholine in propylene glycol) was donated by Lipoid, Germany. Polydimethylsiloxane (PDMS, Sylgard 184) was purchased from Dow Corning, USA.

Construction of MEs using pseudoternary phase diagrams

The solubility of Hy in oils and surfactants was investigated to select the most suitable components for the development of MEs. Hy at 0.1 mg/mL was added to the following compounds: oils (MCT, MCT + Phosal® 50 PG, oleic acid) and surfactants (Tween 20, Tween 80, propylene glycol). The mixtures were vortexed for 3 min and centrifuged at 3000 r/min for 10 min. Then, 10 µL of the supernatant was diluted with 1 mL phosphate-buffered saline (PBS) + 0.2% Tween 20 to determine the amount of Hy by fluorescence spectrophotometry (F-4500, Hitachi, Japan). The experiments were repeated in triplicate.

A mixture of surfactants and co-surfactant (Smix) in a ratio of 3:1 (w/w) was added to the oil phase in weight ratios (O/Smix) of 1:5, 1:10, 1:15, 1:20, 1:25, or 1:30. The resulting mixture was then titrated with the aqueous phase by adding volumes of 500 µL of deionized water with 10% ethanol each time at room temperature. During the titration, the mixture was homogenized by vortexing for 1 min, and the changes in the visual aspect were observed. After the titrations, the proportions of the system components were recorded to construct the pseudo ternary diagram classifying the systems obtained according to visual observation. Only clear dispersions of 100 nm or lower particle size were considered in the ME region of the diagram. The shaded area in each phase diagram was plotted to indicate better microemulsifying efficiency. No heating was applied during the preparation of MEs.

Characterization of MEs

All formulations were characterized by physical appearance, particle size, zeta potential, droplet morphology, solution viscosity, solution pH, and Hy content. Dynamic light scattering (DLS) (Zetasizer Nano S90, Malvern, UK) measurement was employed to determine the hydrodynamic diameter, polydispersity indexes (PDI), and zeta potential; the samples were diluted at the ratio of 1:10 to avoid the effect of multiple scattering. A sample drop diluted in water (1:10) was deposited onto a Formvar and carbon-coated 300-mesh copper grid (Ted Pella Inc., USA) to investigate the ME droplet morphology. After removing the excess and staining with 1% phosphotungstic acid for 30 s, the sample was dried and analyzed by a transmission electron microscope (JEM-2100, Jeol, Japan) operated at 200 kV. The selected MEs were characterized by fluorescence spectroscopy at $\lambda = 553$ nm

(excitation) and $\lambda = 560$–800 nm (emission) using a quartz cuvette with an optical path length of 1 cm.

The electrical conductivities were measured using a DIGIMED® model CD-40 conductometer. The pH of the formulation was measured by a pH-meter (Mettler Toledo MP 220, Switzerland). The viscosity was quantified by Discovery Hybrid Rheometer (DHR-2, TA-Instruments, USA) using 40-mm-diameter parallel plates with a truncation gap of 100 µm. The Hy encapsulation efficiency in MEs was determined by the ultrafiltration method using Amicon® centrifugal filter devices with a 100 kDa molecular weight cut-off membrane (Millipore, USA); Hy-loaded ME at 100 mg/L (1 mL) was added in the upper donor chamber, and the unit was centrifuged at 8000 r/min for 40 min. All of these measurements were performed in triplicate at 25 °C.

The stability of MEs loaded with 100 µg/mL of Hy was monitored over 180 days by checking their droplet size, PDI, zeta potential, hypericin content, and any visual changes.

Singlet oxygen generation

Singlet oxygen ($^1O_2$) generation was analyzed using SOSG. Each sample (free Hy in PBS, DMSO, or Hy-loaded MEs) was added to SOSG at 5 µmol/L for a final Hy concentration of 20 µmol/L. The samples were then irradiated with yellow LED ((590 ± 10) nm) at 8.4 mW/cm^2 for 20 min. SOSG fluorescence at $\lambda = 488/525$ nm (excitation/emission) was monitored using a Synergy H1 hybrid multi-mode reader (BioTek Instruments Inc., USA).

Cell cultures

Mouse malignant melanoma cells (B16F10 cells) and Balb/c mouse 3T3 Clone A31 fibroblasts (3T3 cells) were cultured using DMEM supplemented with 10% FBS, 10,000 U/mL of penicillin and 10 mg/mL of streptomycin. Both cell lines were maintained at 37 °C under 5% CO$_2$ in an incubator.

3D-bioengineered malignant melanoma model using GelMA

GelMA was synthesized according to a previously published protocol [29, 30]. Briefly, porcine skin gelatin was mixed at 10% (w/v) into PBS and stirred at 60 °C until fully dissolved. MA was added to the solution at a rate of 0.5 mL/min until a concentration of 8% (v/v) was obtained in the gelatin solution. The solution was stirred for 1 h at 50 °C, followed by two times dilution with PBS at 50 °C, and then dialyzed against distilled water using 12 kDa cut-off dialysis tubing for one week at 40 °C to remove the unreacted groups from the solution. The GelMA solution was frozen overnight at − 80 °C and lyophilized in a freeze dryer for a week. The dried GelMA was stored at − 20 °C until further usage.

Fig. 1 Schematic process of GelMA molding and cell encapsulation. **a** GelMA pre-polymer synthesized from porcine skin gelatin, which became photocurable by adding 0.3% LAP and irradiation under violet light ($\lambda = 403$ nm). **b** The melanoma (B16F10) and fibroblast (3T3) cells were added to GelMA solution containing 0.3% LAP and cast into a PDMS mold; after crosslinking by violet light, this 3D cell-laden construct was cultured for 14 days to be treated with Hy-loaded MEs following PDT by irradiation with yellow light ($\lambda = 590$ nm)

Figures 1a and 1b illustrate the GelMA fabrication process and the application of Hy-loaded MEs and PDT to the cell-laden constructs. For in vitro 3D constructs, B16F10 and 3T3 cells at 1×10^7 cells/mL of each type were suspended in 6% (w/v) GelMA containing 0.3% LAP (w/v) in PBS, transferred to a PDMS casting mold (8 mm $\times$ 8 mm $\times$ 3 mm), and then photocrosslinked by exposure to violet light ($\lambda = 403$ nm) at an intensity of 40 mW/cm^2 for 15 s. Hydrogel constructs were cultured in DMEM with 10% FBS at 37 °C under 5% CO$_2$ for 14 days. PDT treatment was performed first by incubating the cells with Hy-loaded MEs, and then irradiating them with yellow light ($\lambda = 590$ nm).

Mechanical properties

The fabricated GelMA hydrogels were assessed for their Young's modulus by using a mechanical tester (6800 Series, Instron, USA) with a ramp of 2.0 N/min up to a maximum of 100.0 N. The data were plotted as a stress-strain curve, and the Young's modulus was calculated as the slope of the linear region of this curve between 0 and 20% strain.

Immunofluorescence assay

The cell-laden samples were fixed in 4% (w/v) paraformaldehyde for 15 min and then 0.1% Triton X-100 for 15 min to permeabilize the cell membrane, followed by blocking with 1% (w/v) BSA for 15 min at room temperature. For F-actin cytoskeleton staining, the samples were soaked in a 1:1000 dilution of phalloidin-FITC in 0.1% (w/v) BSA for 1 h. Finally, the nuclei were stained with DAPI for 10 min. For the cell co-culture observation, B16F10 and 3T3 cells in GelMA constructs were marked using two different long-term Cell Trackers, Green CMFDA and Red CMTPX, respectively. The Cell Tracker solutions were prepared according to the manufacturer's protocol. The images were acquired by an inverted fluorescence microscope (Axiovert 200 M, Carl Zeiss, Germany).

Cytotoxicity assay

First, the cytotoxicity of empty MEs and Hy-loaded MEs was evaluated by MTT assay. The Balb/c 3T3 cells or B16F10 cells were seeded in 96-well plates at a density of 1×10^5 cells per well for 24 h. Then, the cells were incubated with different concentrations of formulations prepared in DMEM. After 24 h, this medium was removed, and the cells were washed twice with PBS. Subsequently, 50 μL per well of MTT at 1 mg/mL in culture medium was added to each well. After incubation for 3 h, the medium was removed, and the formazan crystals were dissolved in 50 μL of ethanol, followed by the addition of 150 μL of PBS: isopropanol (1:1) mixture to each well. The absorbance was measured at 570 nm using a microplate reader (Multiskan GO, Thermo Scientific, USA).

For the 3D malignant melanoma model, the Live/Dead Cell Viability Assay kit was used to observe the viability changes in the cells in the culture according to the manufacturer's instructions. The cells were incubated with calcein AM (2 μg/mL in PBS) and ethidium homodimer (4 μg/mL in PBS) reagents for 30 min at 37 °C under light protection. The green and the red fluorescence images of viable and non-viable cells, respectively, were captured using an inverted fluorescence microscope (Axiovert 200 M, Carl Zeiss, Germany).

A CCK-8 assay was further performed to assess the cell viability in 2D and 3D cell-laden constructs after PDT. The free Hy and Hy loaded in M1C and M2A at 0, 1, 50, 100, and 200 nmol/L in DMEM were applied to cells. After 24 h, the medium containing the Hy formulations was removed, and the cells were washed twice with PBS. Afterward, the cells were incubated with 10% CCK-8 in DMEM for 4 h at 37 °C. The absorbance of samples and corresponding controls was determined at 450 nm using a microplate reader (Multiskan GO, Thermo Scientific, USA).

HIF-1α-production in the 3D malignant melanoma model

The cell culture supernatants collected from the 3D malignant melanoma model were centrifuged at 3500 g for 5 min at 4 °C to remove any impurities. The secreted HIF-1α protein was quantified using the HIF-1α ELISA kit according to the manufacturer's protocol. The control was prepared from monolayer cell culture.

Cellular uptake of the Hy-loaded ME in the 3D malignant melanoma model

In order to analyze the cellular internalization of Hy in the 3D melanoma model, the cells were fixed with 4% paraformaldehyde for 20 min, and the nuclei were stained by DAPI for 10 min. Subsequently, the cellular internalization of free Hy and Hy-loaded MEs was analyzed by CLSM (LSM 780, Carl Zeiss, Germany) using the excitation wavelength of 543 nm generated by a He–Ne laser beam. The fluorescence emission of samples was detected at a wavelength of 590 nm.

Statistical analyses

All quantitative data were presented as mean ± standard deviation (SD). One-way ANOVA was used to determine the statistical significance between the experimental groups with the Tukey post-hoc test. Values of *$p < 0.05$, **$p < 0.01$, and ***$p < 0.001$ indicated significance.

Results and discussion

Screening of components for ME

The most crucial criterion for ME development is the selection of the formulation components based on drug solubilization. Therefore, a Hy solubility test at 100 μg/mL was performed in various media. Figure S1 (Supplementary Information) shows that Hy was soluble in all the surfactants and co-surfactant: Tween 80, Tween 20, and propylene glycol. For the oil phase, Hy was entirely soluble in oleic acid and partially soluble in MCT. For the latter medium, 3% Phosal® 50PG was added to fully solubilize Hy. Phosal® 50PG contains phosphatidylcholine, the principal phospholipid in lecithin that functions as an emulsifier [31]. Oleic acid is a hydrophobic biocompatible compound acting as a permeation enhancer due to its partition into the stratum corneum, destabilizing skin lipids [32].

In order to construct ternary phase diagrams, oleic acid was combined with Tween 20 and propylene glycol, while MCT + 3% Phosal® 50PG was combined with Tween 80 and propylene glycol. Subsequently, the ideal combination of surfactants and co-surfactant ratios was determined as 3:1 (w/w) to suit the required HLB values of these oil phases. The final HLB values were identified as up to 10 to generate oil-in-water (O/W) ME, since high solubility leads drug association to the oily phase, and the correct blend of HLB surfactants contributes to the formation of a stable ME upon dilution with water [33]. Meanwhile, the use of co-surfactant such as propylene glycol assists with the decrease in interfacial tension and viscosity. Furthermore, non-ionic surfactants such as Tween 80 and Tween 20 are less toxic than ionic surfactants and have a lower critical micellar concentration, offering stability in a biological environment [34].

Construction of pseudo-ternary phase diagrams and ME characterization

The set of oily phases (O) and the mixture of surfactant and co-surfactant (Smix) were titrated with the aqueous phase (W) using deionized water + 10% ethanol. Based on the preliminary screenings, the domain of the points was delimited, in which the maximum solubilization of the dispersed phase forms a homogeneous, transparent, translucent, and isotropic system, a typical characteristic of ME. Figure 2a shows the pseudo-ternary phase diagrams, in which the formulations M1C and M2A were selected due to their maximum water content and lowest possible surfactant content.

The obtained diagrams were compared to observe the effects of surfactants with different HLB values on the ME region. The higher HLB value of Tween 20 (HLB = 16.7) was optimal to incorporate a more aqueous phase because it enhances interfacial layer hydrophilicity [33]. Meanwhile,
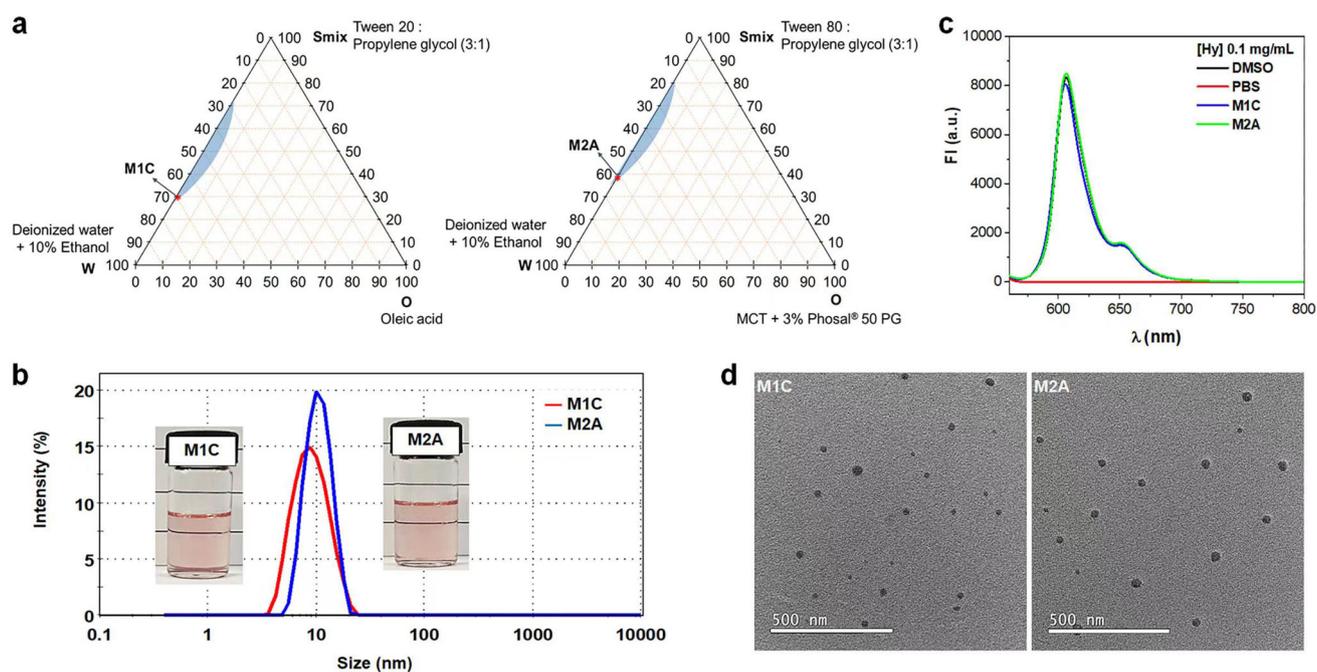
Fig. 2 a Pseudo-ternary phase diagrams depicting the influence of oil phase composition on ME formation: W = aqueous phase, Smix = mixture of surfactant and co-surfactant, O = Oil phase. The isotropic MEs selected for dynamic light scattering analysis were: 1) M1C (W = deionized water + 10% ethanol, Smix = Tween 20: propylene glycol (3:1), O = Oleic acid); 2) M2A (W = deionized water + 10% ethanol, Smix = Tween 80: propylene glycol (3:1), O = MCT + 3% Phosal® 50PG). The dark area corresponds to the ME formation area. **b** Droplet size distribution of Hy-loaded MEs: M1C and M2A by DLS. **c** Hypericin fluorescence spectra at 0.1 mg/mL in different media: PBS, DMSO, M1C, and M2A obtained with excitation at 552 nm and emission at 560−800 nm. **d** TEM images of phosphotungstic acid staining of M1C and M2A

Tween 80 (HLB = 15) is less hydrophilic, decreasing the partition into the aqueous phase, thus reducing the water loading and narrowing the ME region. Figure 2b shows the droplet size distribution of the selected MEs. All MEs had a droplet size of approximately 10 nm. However, M1C formulated with oleic acid showed the widest range of droplet sizes in the sample. This might be due to the carbon chain of oleic acid (18 carbons) including a double bond, whereas MCT is usually composed of short chains with 6–12 carbons. The number of carbons in the compounds used for the oil phase can influence the emulsification process, since long chains have difficulty in penetrating the interface of the surfactants and are usually dispersed [35].

The fluorescence emission spectra obtained for 0.1 mg/mL Hy in DMSO, PBS, M1C, and M2A (Fig. 2c) showed that Hy-loaded MEs presented similar fluorescence emissions to Hy in DMSO, since this is the most used solvent for Hy stock solution preparation. Conversely, Hy is insoluble in PBS and aggregates in aqueous media to yield low fluorescence emission. It can be concluded that the prepared MEs were efficient in Hy solubilization. Figure 2d shows the images obtained from transmission electron microscopy, revealing that the lipid droplets were spherical. These results corroborate the droplet size analysis, showing that droplets are present in

the nanometer range and have varying sizes from approximately 10 nm. Table 1 details the characteristics of selected MEs. The selected ME displays an internal phase diameter range from 8 to 14 nm (with PDI < 0.2) and a negative zeta potential (about − 10 mV), suggesting formulation stability. The zeta potential represents the total charge of the lipid vesicle or particle in a medium. Zeta potential values equal to or greater than 30 mV (module) are considered stable, which is mainly true for particulate systems. However, this rule may not be valid for some ME formulations with a lower

Table 1 Characteristics of selected MEs

Microemulsion	M1C	M2A
Particle size (nm)	8.38 ± 0.13	10.39 ± 0.04
PDI	0.141 ± 0.047	0.021 ± 0.011
Zeta potential (mV)	− 9.62 ± 1.12	− 11.7 ± 1.83
pH	4.99 ± 0.13	6.83 ± 0.21
Conductivity (µS/cm)	301.2 ± 0.5	203.5 ± 0.2
Viscosity (Pa s)	0.003 ± 0.001	0.132 ± 0.001
Encapsulation efficiency (%)	88.45 ± 3.92	87.43 ± 2.70

zeta potential [36]. In general, dispersed droplets are stable when enough electrostatic repulsion between them is allied to some steric impediment. These associated phenomena reveal that intermediate zeta potential values can avoid the aggregation of droplets from MEs, increasing their stability. Thus, the stability of MEs containing non-ionic surfactants in their composition, such as that of the formulations of the present study, does not depend only on the zeta potential, because its stability is significantly influenced by the surfactant chain size [37]. The obtained values for the electrical conductivity of the MEs were in the order of 100 μS/cm, indicating that the emulsion type was O/W. The conductivity was measured to determine the type of ME and estimate the predominant phase resulting from the changes in composition or temperature. The actual value mainly reveals whether this phase is aqueous or oily, or both phases are continuous. Microemulsified O/W and bi-continuous systems have higher electrical conductivity values than microemulsified type W/O systems. O/W MEs are preferred in biological applications, as the oil nanodroplets dispersed in water can offer excellent capacity to solubilize hydrophobic compounds and increase their stability and bioavailability [38]. To determine the Hy encapsulation efficiency present in MEs, separating the non-encapsulated fraction using high-speed spin centrifugation (11 000 g) was necessary. Both selected MEs had > 80% encapsulation efficiency, meaning that the formulations efficiently encapsulated Hy at 100 μg/mL.

The physicochemical stability of the MEs after 6 months of storage at temperatures 4, 25, and 37 °C is shown in Fig. S2 (Supplementary Information). At 4 and 25 °C, the MEs demonstrated isotropic and translucent morphology, as shown by macroscopic visualization during this period. In addition, the droplets maintained their initial sizes and PDIs with no evidence of precipitation or flocculation. The initial concentration of Hy encapsulated in these ME systems also remained constant, showing that the compound was thermostable in the MEs. However, the increase in PDI values was observed under storage at 37 °C, which might be due to the dehydration of the formulation that altered the interfacial tension and increased the kinetic energy between the droplets, so that they could overcome the energy barrier and tend to get closer to each other, provoking flocculation and coalescence [39]. Despite the instability of MEs when stored at 37 °C, the thermodynamic stability of MEs still contributed to the conservation of nanodroplet sizes at 4 and 25 °C. These temperatures offer advantages over unstable dispersions, such as suspensions and macroemulsions, by providing a much longer shelf life.

Singlet oxygen generation

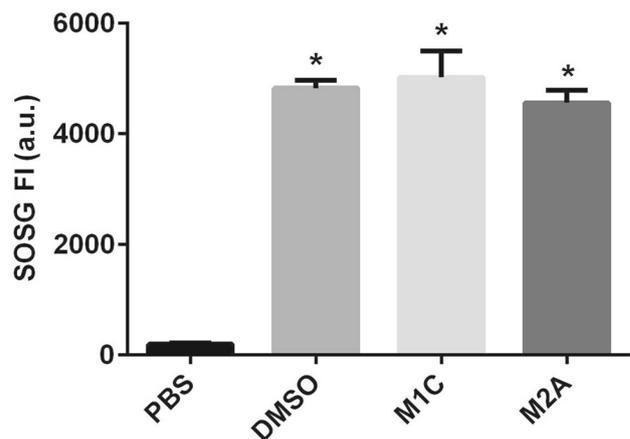The efficiency of Hy-loaded MEs to generate $^1O_2$ was analyzed using the SOSG reagent. As shown in Fig. 3, strong

Fig. 3 $^1O_2$ generation by Hy (20 μmol/L) in different media: PBS, DMSO, M1C, and M2A after irradiation with light at 590 nm (light dose: 10 J/cm^2). The fluorescence intensity (FI) of SOSG probe was detected by excitation and emission wavelengths at 504 and 525 nm, respectively. Significant difference (*$p < 0.001$) was found against PBS

SOSG fluorescence intensity of the free Hy in DMSO or Hy-loaded MEs was observed upon 590 nm yellow LED irradiation for 20 min. On the contrary, Hy was insoluble in PBS, leading to precipitation and low SOSG fluorescence. The low solubility of Hy in an aqueous medium makes it form self-aggregates that reduce the fluorescence quantum yield, resulting in the difficulty to transfer energy from triplet state to oxygen, thus undermining the process of $^1O_2$ generation [40]. Although the MEs contain 60%–70% of water, the nanodroplets of oil stabilized by the surfactants enable Hy to be water soluble. This fact markedly increases Hy bioavailability, since $^1O_2$ generated after light irradiation in the presence of oxygen promotes the oxidation of surrounding biomolecules, damages the vascular system, and triggers programmed cell death by apoptosis [41].

Bioengineered 3D malignant melanoma model

The cell encapsulation condition in GelMA was first investigated by loading the cells into 6%, 8%, or 10% (w/v) GelMA pre-polymer followed by violet light crosslinking. This process generates a stable 3D construct at 37 °C. The optical images in Fig. 4a show that the cells only stretched and exhibited vigorous spreading in 6% GelMA after 3 days. In comparison, spherical cell morphologies were observed at higher GelMA concentrations (8% and 10%). Indeed, cells can suffer stress during the encapsulation process; especially, an elevated GelMA concentration turns the scaffold into a rigid and compact solid with inadequate porosity and transient swelling in the culture medium for cell proliferation because of the poor supply of nutrients and oxygen in 3D cell culture [42]. GelMA can be attributed tunable properties by modifying the concentrations of its constituents, its

Fig. 4 a Optical micrographs showing cells spreading in the cell co-culture of B16F10 and 3T3 cells in 6%, 8%, and 10% (w/v) GelMA followed by violet light irradiation at 40 mW/cm^2 for 15 s (Scale bar = 100 µm). **b** Stress-strain curves of 6%, 8%, and 10% (w/v) GelMA hydrogels. **c** Calculated Young's moduli. The data are expressed as mean ± SD ($n = 3$). *$p <$ 0.05, **$p <$ 0.01, ***$p <$ 0.001
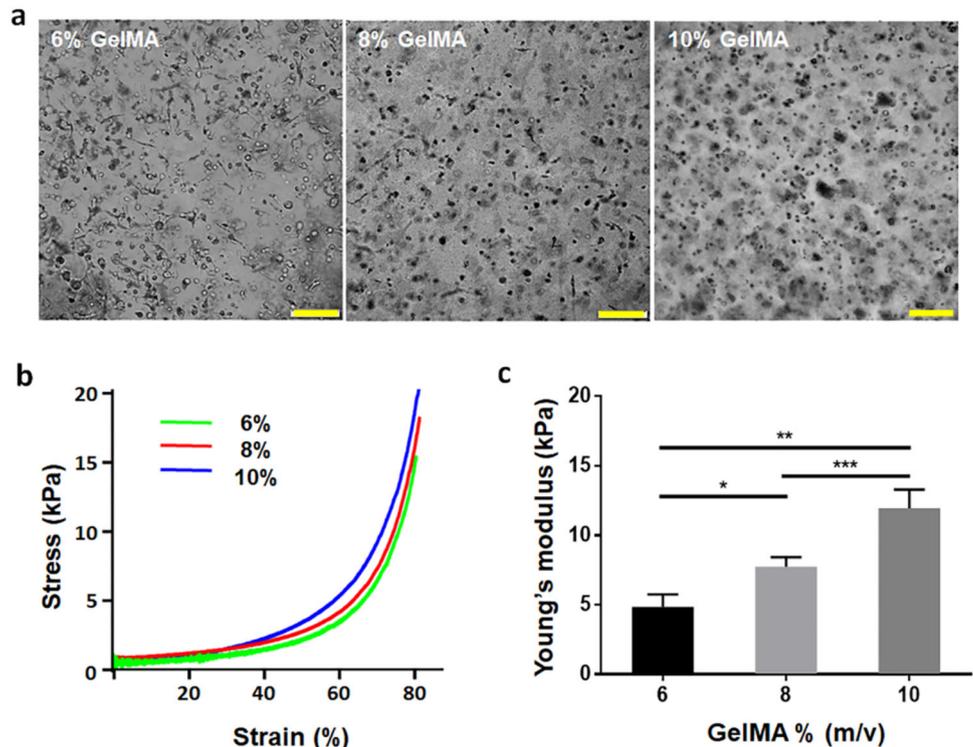
synthesis process and crosslinking parameters to achieve a desirable condition for the culture of different cell types and physiological applications [43].

Encapsulating cells into GelMA allows cell adhesion, proliferation and differentiation in an extracellular environment [44]. Other traditional cell-laden biomaterials like Matrigel, collagen and decellularized extracellular matrices are typical animal-derived scaffolding elements composed of various polysaccharides, proteins (e.g., collagen and laminin) and growth factors. Compared to these, GelMA holds relatively tunable mechanical properties and sufficient stability due to the temperature-independent and irreversible photocrosslinking process. GelMA also provides the advantage of improving the control of batch-to-batch variability while being more economical than these matrices [45].

Another interesting advantage revealed in our study while working with PDMS molds is that GelMA is more straightforward to handle and utilize for modeling 3D constructs with tailorable dimensions and thickness, rendering it an effective tissue-engineering platform for drug screening. This robust replication method can also enable the rapid creation of tumor models on a patient-specific basis to evaluate treatments without requiring sophisticated technological equipment such as a 3D bioprinter.

The mechanical properties of GelMA were further described (Fig. 4b). The Young's moduli of GelMA at 6%, 8% and 10% (w/v) were (4.84 ± 0.51), (7.73 ± 0.39) and (11.94 ± 0.78) kPa, respectively (Fig. 4c). As depicted, the

change in stiffness of GelMA can be achieved by modulating its concentration. In addition, our result demonstrated that using 6% (w/v) GelMA for melanoma and fibroblast cell co-culture provided a similar stiffer environment comparable to previously reported human skin with Young's moduli between 4.5 and 8 kPa [46]. Another in vivo study using nude mice also demonstrated that the Young's modulus of melanoma tissue was higher than that of non-melanoma ((4.93 ± 2.38) vs. (0.98 ± 0.41) kPa) [47]. The stiffer environment of melanoma resembles solid tumors and is better mimicked using denser GelMA gels. Malignant transformation is accompanied by specific signaling in cellular and extracellular mechanical properties, such as stiffness and adhesion. Several studies reported that mechanical regulation influences tumor growth and hypoxic core formation inside the tumor mass, thus contributing to drug resistance while displaying an increased stiffness compared to normal tissues [48].

The cell viability of 3D cell co-culture (B16F10 and 3T3 cells) in 6% (w/v) GelMA was verified by live/dead staining (Fig. 5a). Most of the cells were viable over 14 days of culture, which also demonstrated that the cells readily proliferated and elongated in GelMA scaffolds. Since GelMA is a photocurable hydrogel that is widely used as a 3D cell culture matrix, its tunable mechanical properties enable the creation of complex, cell-responsive microtissues [49]. Moreover, as shown in Figs. 5b and 5c, increased F-actin filamentous networks within the cells evidenced that the co-culture of
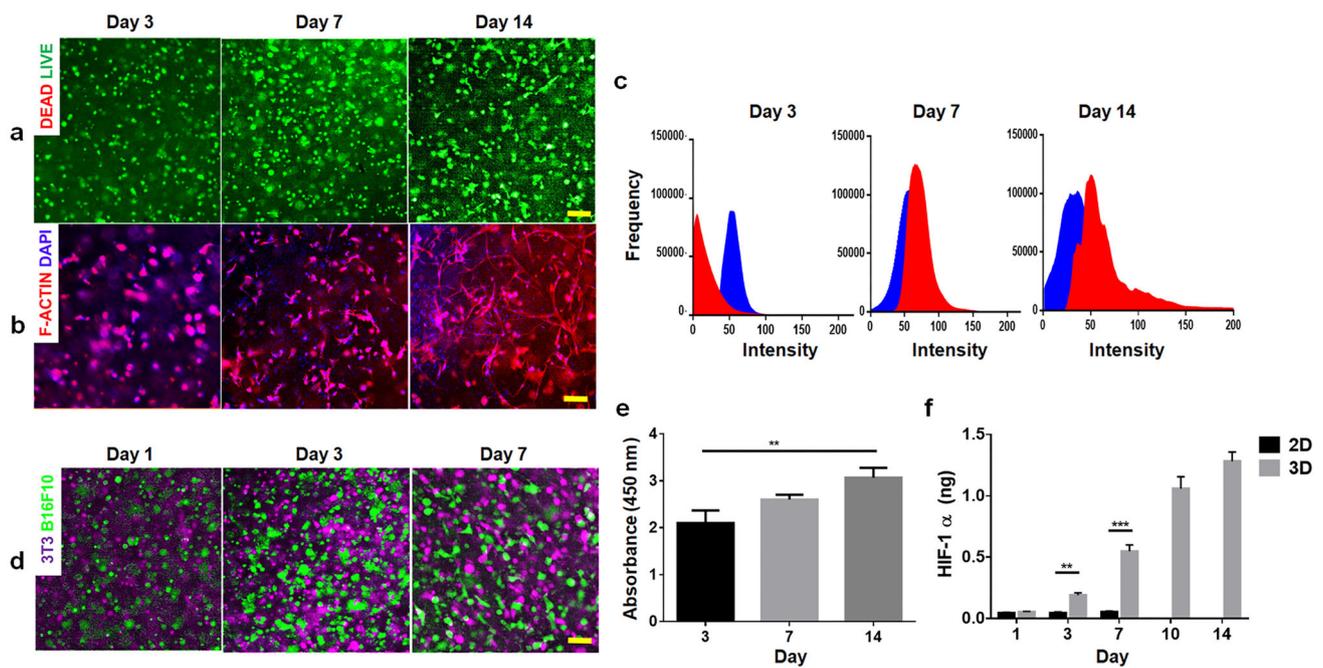
Fig. 5 Immunostaining assay was conducted to observe cell viability and cell spreading in the co-culture of 3T3 and B16F10 cells in 6% GelMA + 0.3% LAP. **a** Live/Dead cell staining. Scale bar = 500 μm. **b** F-actin/nuclei staining by phalloidin-FITC/ DAPI at 3, 7, and 14 days. Scale bar = 500 μm. **c** F-actin/nuclei fluorescence intensity over 14 days. **d** B16F10 cells (green color) and 3T3 cells (magenta color) were marked with Cell Trackers CMTPX and CMFDA, respectively. Scale bar = 500 μm. **e** CCK-8 assay showing increased cell proliferation in the photocrosslinked GelMA. **f** The HIF-1α expressions were measured after 1, 3 and 7 days for the 2D model and after 1, 3, 7, 10, and 14 days for the 3D model. The data are expressed as mean ± SD ($n = 3$). *$p < 0.05$, **$p < 0.01$, ***$p < 0.001$

B16F10 and 3T3 cells could promote the cytoskeleton organization supported by the interactions between the two cell types and between cells and GelMA. Numerous in vitro studies have indicated that the F-actin networks have a unique molecular signature for creating a dynamic structure in 3D cell culture, which can generate mechanical behaviors by modulating cell adhesion, migration, and division [50, 51].

The cell co-culture of B16F10 and 3T3 cells was examined using two different long-term Cell Trackers. The cells were first marked and then mixed into 6% GelMA. Figure 5d shows the monitoring results for both cell lines over 7 days. It was found that the GelMA scaffolds allowed the maintenance of cellular interactions to ensure their proper growth. Fibroblasts, as the main cellular components within the tumor stroma, have been reported to promote the dynamic interactions of tumor cells with acellular components that contribute to extracellular matrix formation and stimulate cell–cell interactions as well as cell growth and invasion [52]. In addition, fibroblasts can protect cancer cells from immune defense [53]. These features tremendously affect tumor morphology and gene expression and increase resistance to chemotherapy and radiotherapy [54, 55]. Thus, many studies also focused on targeting tumor-associated fibroblasts for developing novel cancer therapies [56]. All of these data suggest that the co-culture melanoma model better reflects

the actual in vivo tumor-stromal architecture and provides a promising approach for predicting the antitumor efficacy of drug candidates.

The cell metabolic activities were verified by the CCK-8 assay (Fig. 5e). The results showed that metabolic activity increased over time in 3D cell co-culture, providing evidence that the GelMA construct created a cell-proliferative milieu with cell-adhesive domains such as RGD, and was sufficient to support the growth of the co-culture of melanoma and fibroblast cells over prolonged periods. The cell metabolic activities were also corroborated by Live/Dead assay, since no significant cell death was observed at 14 days of culture. Besides, GelMA crosslinked by violet irradiation during 15 s (0.6 J/cm^2) did not significantly affect cell viability or the metabolic activities.

The hypoxia inside 2D and 3D cell co-culture was detected by ELISA assay for HIF-1α released in the supernatant of the culture medium (Fig. 5f). At 24 h, the concentrations of HIF-1α were similar in both systems. However, the HIF-1α level in 3D cell culture was significantly higher for longer incubations than in 2D, and the latter contained very low detectable HIF-1α. Since the cell viability in 2D was considerably affected by long-term cultivation (> 7 days) due to the lack of space for cell growth, we did not quantify HIF-1α at 10 and 14 days.
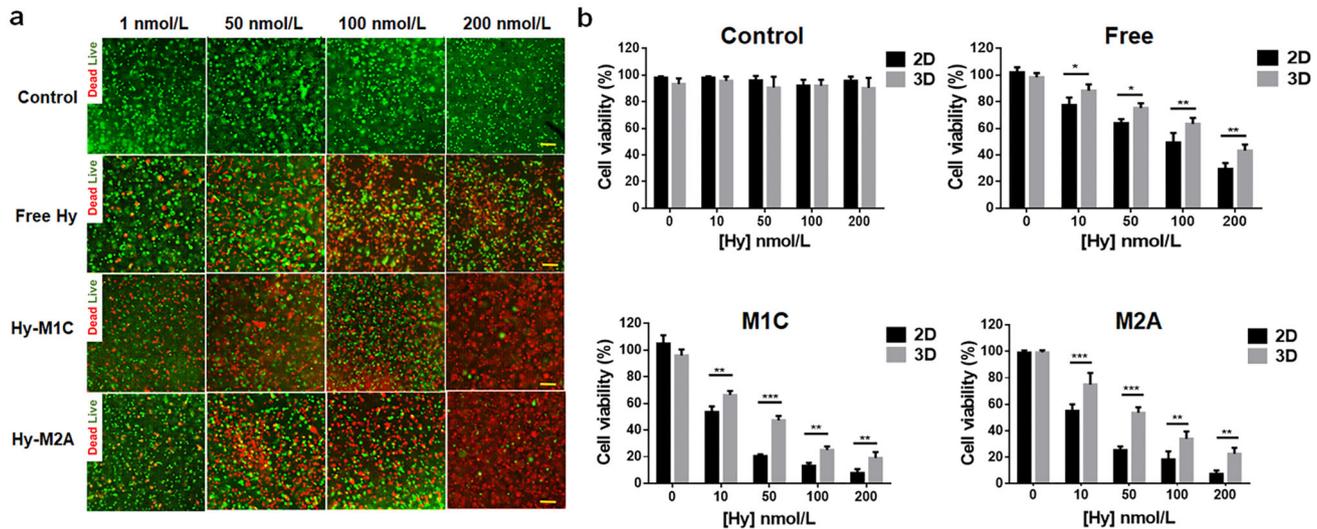
Fig. 6 a Live/Dead cell staining of 3D malignant melanoma models. Cells were treated with free Hy and Hy loaded in M1C and M2A (from 1 to 200 nmol/L), followed by PDT (yellow-light irradiation at 10 J/cm^2). Red color denotes a dead cell, and green denotes a live cell. Scale bar = 300 μm. **b** The metabolic activity and cell death in 2D and 3D cell cultures after Hy-PDT were determined by CCK-8 assay. The data are expressed as mean ± SD ($n = 3$). *$p < 0.05$, **$p < 0.01$, ***$p < 0.001$

As expected, hypoxic conditions are hard to reproduce in classic 2D cell culture. Conventional 2D culture substrates like tissue culture polystyrene flasks present significant drawbacks limiting how the study conclusions can appropriately be translated to actual in vivo processes. On the other hand, in a complex 3D microenvironment, melanoma grows in a stromal mimicry in 3D spatial conformation where cells are subjected to long-term culture and the stiffness of GelMA support. A hypoxic core occurs in response to heterogeneous oxygen gradients, promoting the release of soluble signals such as HIF-1α, which have a crucial tumor pathological aspect of inducing cell migration and invasion; it allows efficient cellular cross-talk for assessing therapy responses to signaling inhibitors [57].

Cytotoxicity evaluation for 2D and 3D cell co-culture melanoma models

The cytotoxicity of empty MEs was investigated by the MTT assay (Fig. S3 in Supplementary Information). The empty MEs exhibited no significant effect on the survival rate of Balb/c 3T3 and B16F10 cells at 10 mg/mL in the culture medium, and the cell survival rate was above 90%. In PDT treatment, 3D models were incubated with free Hy and Hy-loaded MEs at 0, 1, 50, 100, and 200 nmol/L for 24 h, followed by yellow LED irradiation at 10 J/cm^2. For the 3D model, the Live/Dead staining result is shown in Fig. 6a; the MEs containing Hy exhibited more pronounced and significantly higher phototoxicity (about threefold) ($p < 0.05$) than the free Hy. In addition, the cell metabolic activities were verified by the colorimetric CCK-8 assay (Fig. 6b) to better

compare 2D and 3D cell cultures, which indicated that the cells cultured in the 3D system displayed less susceptibility (at least about 2.5-fold) to the PDT treatment than those in the 2D system.

The fibroblasts and melanoma cells co-embedded in GelMA enabled them to mimic the 3D structure organization, creating heterogeneous growth states for both cell lines. In addition, the hypoxic core occurring in the 3D cell culture may induce the most cells within this region to divide or undergo apoptosis; therefore, the malignant cells found at the periphery show the highest level of cell proliferation and become more invasive when supported by GelMA construct and stromal cells such as fibroblasts [58, 59]. The upregulation of metabolic expression related to HIF on melanoma cells grown in 3D has been reported as one of the significant drawbacks of this platform to evaluate therapeutic agents, since 3D cell cultures are heterogeneously exposed to oxygen, nutrients and drugs; therefore, these hypoxic micro-tumors are mostly negatively susceptive to drugs and contribute to developing drug-resistance [60]. Thus, the use of GelMA to recreate functional 3D malignant melanoma models enables the recapitulation of a relevant cellular condition to reflect native tissue morphology and contributes to the improved predictability of drug efficacy over traditional 2D cultures.

Cell uptake of Hy-loaded MEs against 3D melanoma models

The 3D melanoma model was used to evaluate the penetration of Hy from MEs. CLSM was used to analyze its
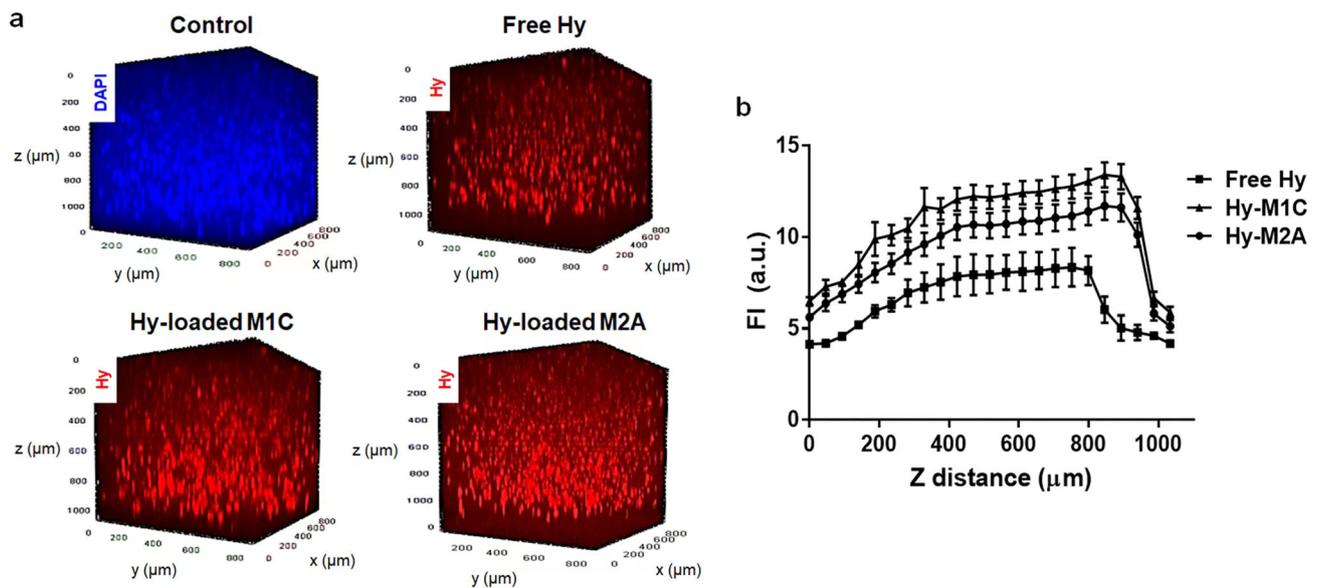
Fig. 7 a Using CLSM to evaluate the penetration of free Hy and Hy-loaded MEs in the 3D malignant melanoma model. The red dot represents the penetrated Hy, while the DAPI-nuclei staining represents the control (blue color). **b** Quantification of Hy fluorescence intensity over the Z distance measured from the total of 23 slices; the average fluorescence of each slice for an in vitro tissue depth of 47.01 μm was calculated ($n = 3$)

full thickness to detect Hy fluorescence over the Z-distance. Figures 7a and 7b display 3D reconstructions from the multilayer scanning of Hy fluorescence and their corresponding quantifications. The details of Hy fluorescence of each layer are presented in Fig. S4 (Supplementary Information). In general, Hy-loaded MEs demonstrated higher penetration than the free Hy (about 2.5-fold) ($p < 0.05$). Reports have shown that the ME acts as a penetration-enhancer in the skin and tumor tissues, since the hydrophobic drug is encapsulated into an oil core stabilized by an interfacial film of amphiphilic surfactant molecules, increasing the partition of the drug into the membrane [39, 61]. Although the difference in particle sizes between the M1C and M2A did not show a significant influence on Hy penetration, the higher water content of M1C (68%) compared to M2A (58%) may assist in decreasing viscosity, consequently increasing drug diffusion, release and transport across the membrane [62].

The cellular internalization of Hy can be attributed to the fact that cancer cells express a high number of low-density lipoprotein (LDL) receptors compared to normal cells [63]. Therefore, the ME inner core composed of triglycerides and cholesterol esters has a high affinity to LDL receptors on cultured B16F10 cells [64]. The intracellular accumulation of Hy via LDL receptors could be in turn more intense in malignant melanoma cells. Although this targeted feature of Hy-loaded MEs could diminish Hy-accumulation in healthy 3T3 cells, we still found a significant difference

in photocytotoxicity compared to free Hy for 2D and 3D melanoma models. The results here highlight the advantage of Hy-loaded MEs over the free formulation for tissue penetration, potentially eradicating the pathological tissue by PDT in melanoma treatment.

It is worthy to note that the production of the GelMA-based 3D melanoma model was readily attainable, with reproducible constructs for use as a potential replacement to in vivo models in preclinical testing. Besides, high-throughput screening leverages significant and robust findings for translation to clinically observed drug penetration involved in the pathway of different drug-delivery strategies. Moreover, CLSM imaging techniques allow for qualitative and quantitative fluorescent drug detection in 3D cell constructs, offering a valuable tool to rapidly analyze drug uptake by cells and prove the therapeutic outcome in melanoma.

Conclusions

In this study, the co-culture of melanoma and fibroblast cell-laden constructs fabricated using GelMA and photopolymerization yielded a reliable 3D malignant melanoma model owing to similarities to the native counterpart, including F-actin networks, HIF-1α expression, and tissue mechanical properties. The Hy-loaded MEs were successfully developed and tested directly in these 3D models, which showed more resistance to Hy-PDT than the traditional 2D cell culture. Using confocal microscopy, the penetration of Hy could be

conveniently visualized by Z-step scanning while measuring the Hy fluorescence intensity. The phototoxicity and penetration of Hy-loaded MEs were more potent than those of free Hy, indicating that Hy nanodroplets could penetrate tumor tissue more efficiently. Our results suggest that this tissue-engineered in vitro model platform can be an ethically acceptable approach to investigate drug-tissue interactions and provide a basis for evaluating nanocarrier efficacies for skin cancer and other skin-related diseases.

Author contributions HLM: conceptualization, methodology, visualization, investigation, writing—original draft preparation. WL: conceptualization, methodology. MW: methodology. LCV: methodology, writing—review & editing. JRP: resources. YSZ: conceptualization, methodology, writing—review & editing, supervision. EC: conceptualization, writing—review & editing, project administration, resources, supervision.

Declarations

Conflict of interest The authors declare that there is no conflict of interest.

Ethical approval This article does not contain any studies with human or animal subjects performed by any of the authors.

References

1. Schadendorf D, van Akkooi AC, Berking C et al (2018) Melanoma. Lancet 392:971–984. https://doi.org/10.1016/S0140-6736(18)31559-9
2. Gordon R (2013) Skin cancer: an overview of epidemiology and risk factors. Semin Oncol Nurs 29(3):160–169. https://doi.org/10.1016/j.soncn.2013.06.002
3. Cummins DL, Cummins JM, Pantle H et al (2006) Cutaneous malignant melanoma. Mayo Clin Proc 81(4):500–507. https://doi.org/10.4065/81.4.500
4. Atallah E, Flaherty L (2005) Treatment of metastatic malignant melanoma. Curr Treat Options Oncol 6:185–193. https://doi.org/10.1007/s11864-005-0002-5
5. Domingues B, Lopes JM, Soares P et al (2018) Melanoma treatment in review. ImmunoTargets Ther 7:35. https://doi.org/10.2147/ITT.S134842
6. Dolmans DE, Fukumura D, Jain RK (2003) Photodynamic therapy for cancer. Nat Rev Cancer 3(5):380. https://doi.org/10.1038/nrc1071
7. Zhang L, Ji Z, Zhang J et al (2019) Photodynamic therapy enhances skin cancer chemotherapy effects through autophagy regulation. Photodiagnosis Photodyn Ther 28:159–165. https://doi.org/10.1016/j.pdpdt.2019.08.023
8. Driehuis E, Spelier S, Beltrán Hernández I et al (2019) Patient-derived head and neck cancer organoids recapitulate EGFR expression levels of respective tissues and are responsive to EGFR-targeted photodynamic therapy. J Clin Med 8:1880. https://doi.org/10.3390/jcm8111880
9. Banerjee SM, MacRobert AJ, Mosse CA et al (2017) Photodynamic therapy: inception to application in breast cancer. Breast 31:105–113. https://doi.org/10.1016/j.breast.2016.09.016
10. de Albuquerque IO, Nunes J, Figueiró Longo JP et al (2019) Photodynamic therapy in superficial basal cell carcinoma treatment. Photodiagnosis Photodyn Ther 27:428–432. https://doi.org/10.1016/j.pdpdt.2019.07.017
11. Austin E, Mamalis A, Ho D et al (2017) Laser and light-based therapy for cutaneous and soft-tissue metastases of malignant melanoma: a systematic review. Arch Dermatol Res 309:229–242. https://doi.org/10.1007/s00403-017-1720-9
12. Agostinis P, Vantieghem A, Merlevede W et al (2002) Hypericin in cancer treatment: more light on the way. Int J Biochem Cell Biol 34:221–241. https://doi.org/10.1016/S1357-2725(01)00126-1
13. Jürgenliemk G, Nahrstedt A (2003) Dissolution, solubility and cooperativity of phenolic compounds from *hypericum perforatum* L. in aqueous systems. Pharmazie 58:200–203
14. Callender SP, Mathews JA, Kobernyk K et al (2017) Microemulsion utility in pharmaceuticals: implications for multi-drug delivery. Int J Pharmaceut 526:425–442. https://doi.org/10.1016/j.ijpharm.2017.05.005
15. Jadhav KR, Shaikh IM, Ambade KW et al (2006) Applications of microemulsion based drug delivery system. Curr Drug Deliv 3:267–273. https://doi.org/10.2174/156720106777731118
16. Hu L, Yang J, Liu W et al (2011) Preparation and evaluation of ibuprofen-loaded microemulsion for improvement of oral bioavailability. Drug Deliv 18:90–95. https://doi.org/10.3109/10717544.2010.522613
17. Aboumanei MH, Abdelbary AA, Ibrahim IT et al (2018) Design and development of microemulsion systems of a new antineoplaston A10 analog for enhanced intravenous antitumor activity: in vitro characterization, molecular docking, 125I-radiolabeling and in vivo biodistribution studies. Int J Pharm 545:240–253. https://doi.org/10.1016/j.ijpharm.2018.05.010
18. Ryu KA, Park PJ, Kim SB et al (2020) Topical delivery of coenzyme q10-loaded microemulsion for skin regeneration. Pharmaceutics 12:332. https://doi.org/10.3390/pharmaceutics12040332
19. Benbow T, Campbell J (2019) Microemulsions as transdermal drug delivery systems for nonsteroidal anti-inflammatory drugs (NSAIDs): a literature review. Drug Dev Indl Pharm 45:1849–1855. https://doi.org/10.1080/03639045.2019.1680996
20. Beaumont KA, Mohana-Kumaran N, Haass NK (2014) Modeling melanoma in vitro and in vivo. Healthcare 2:27–46. https://doi.org/10.3390/healthcare2010027
21. Fennema E, Rivron N, Rouwkema J et al (2013) Spheroid culture as a tool for creating 3D complex tissues. Trends Biotechnol 31:108–115. https://doi.org/10.1016/j.tibtech.2012.12.003
22. Hill DS, Robinson ND, Caley MP et al (2015) A novel fully humanized 3D skin equivalent to model early melanoma invasion. Mol Cancer Ther 14:2665–2673. https://doi.org/10.1158/1535-7163.MCT-05-0313
23. Yue K, Li X, Schrobback K et al (2017) Structural analysis of photocrosslinkable methacryloyl-modified protein derivatives. Biomaterials 139:163–171. https://doi.org/10.1016/j.biomaterials.2017.04.050
24. Gungor-Ozkerim PS, Inci I, Zhang YS et al (2018) Bioinks for 3D bioprinting: an overview. Biomater Sci 6:915–946. https://doi.org/10.1039/C7BM00765E

25. Ying G, Jiang N, Yu C et al (2018) Three-dimensional bioprinting of gelatin methacryloyl (GelMA). Bio-Des Manuf 1:215–224. https://doi.org/10.1007/s42242-018-0028-8

26. Murekatete B, Shokoohmand A, McGovern J et al (2018) Targeting insulin-like growth factor-I and extracellular matrix interactions in melanoma progression. Sci Rep 8:583. https://doi.org/10.1038/s41598-017-19073-4

27. Morales D, Lombart F, Truchot A et al (2019) 3D coculture models underline metastatic melanoma cell sensitivity to vemurafenib. Tissue Eng Part A 25:1116–1126. https://doi.org/10.1089/ten.tea.2018.0210

28. Huang LF, Wang ZH, Chen SL (2014) Hypericin: chemical synthesis and biosynthesis. Chin J Nat Med 12:81–88. https://doi.org/10.1016/S1875-5364(14)60014-5

29. Gong J, Schuurmans CCL, Genderen AMV et al (2020) Complexation-induced resolution enhancement of 3D-printed hydrogel constructs. Nat Commun 11:1267. https://doi.org/10.1038/s41467-020-14997-4

30. Huang D, Liu T, Liao J et al (2021) Reversed-engineered human alveolar lung-on-a-chip model. Proc Nat Acad Sci 118:e2016146118. https://doi.org/10.1073/pnas.2016146118

31. Rydhag L, Wilton I (1981) The function of phospholipids of soybean lecithin in emulsions. J Am Oil Chem Soc 58:830–837. https://doi.org/10.1007/bf02665591

32. Boelsma E, Tanojo H, Boddé HE et al (1996) Assessment of the potential irritancy of oleic acid on human skin: evaluation in vitro and in vivo. Toxicol Vitro 10:729–742. https://doi.org/10.1016/S0887-2333(96)00053-7

33. Schmidts T, Dobler D, Nissing C et al (2018) Effects of HLB value on oil-in-water emulsions: droplet size, rheological behavior, zeta-potential, and creaming index. J Ind Eng Chem 67:123–131. https://doi.org/10.1016/j.jiec.2018.06.022

34. Courtney DL Sr (2017) Emulsifier selection/HLB. Surfactants in Cosmetics, Routledge, UK

35. Roohinejad S, Oey I, Wen J et al (2015) Formulation of oil-in-water β-carotene microemulsions: effect of oil type and fatty acid chain length. Food Chem 174:270–278. https://doi.org/10.1016/j.foodchem.2014.11.056

36. Schwuger MJ, Stickdorn K, Schomaecker R (1995) Microemulsions in technical processes. Chem Rev 95:849–864. https://doi.org/10.1021/cr00036a003

37. McClements DJ (2012) Nanoemulsions versus microemulsions: terminology, differences, and similarities. Soft Matter 8:1719–1729. https://doi.org/10.1039/C2SM06903B

38. Warisnoicharoen W, Lansley AB, Lawrence MJ (2000) Nonionic oil-in-water microemulsions: the effect of oil type on phase behaviour. Int J Pharm 198:7–27. https://doi.org/10.1016/s0378-5173(99)00406-8

39. Egito EST, Amaral-Machado L, Alencar EN et al (2020) Microemulsion systems: from the design and architecture to the building of a new delivery system for multiple-route drug delivery. Drug Deliv Transl Res 11:1–26. https://doi.org/10.1007/s13346-020-00872-8

40. Bánó G, Staničová J, Jancura D et al (2011) On the diffusion of hypericin in dimethylsulfoxide/water mixtures—the effect of aggregation. J Phys Chem B 115:2417–2423. https://doi.org/10.1021/jp109661c

41. dos Santos AIF, de Almeida DRQ, Terra LF et al (2019) Photodynamic therapy in cancer treatment-an update review. J Cancer Metastasis Treat 5:25. https://doi.org/10.20517/2394-4722.2018.83

42. Nichol JW, Koshy ST, Bae H et al (2010) Cell-laden microengineered gelatin methacrylate hydrogels. Biomaterials 31:5536–5544. https://doi.org/10.1016/j.biomaterials.2010.03.064

43. Pepelanova I, Kruppa K, Scheper T et al (2018) Gelatin-methacryloyl (GelMA) hydrogels with defined degree of functionalization as a versatile toolkit for 3D cell culture and extrusion bioprinting. Bioengineering 5:55. https://doi.org/10.3390/bioengineering5030055

44. Sun M, Sun X, Wang Z et al (2018) Synthesis and properties of gelatin methacryloyl (GelMA) hydrogels and their recent applications in load-bearing tissue. Polymers 10:1290. https://doi.org/10.3390/polym10111290

45. Aisenbrey EA, Murphy WL (2020) Synthetic alternatives to Matrigel. Nat Rev Mater 5:539–551. https://doi.org/10.1038/s41578-020-0199-8

46. Pailler-Mattei C, Bec S, Zahouani H (2008) In vivo measurements of the elastic mechanical properties of human skin by indentation tests. Med Eng Phys 30:599–606. https://doi.org/10.1016/j.medengphy.2007.06.011

47. Sarna M, Krzykawska-Serda M, Jakubowska M et al (2019) Melanin presence inhibits melanoma cell spread in mice in a unique mechanical fashion. Sci Rep 9:1–9. https://doi.org/10.1038/s41598-019-45643-9

48. Schmid R, Schmidt SK, Hazur J et al (2020) Comparison of hydrogels for the development of well-defined 3D cancer models of breast cancer and melanoma. Cancers 12:2320. https://doi.org/10.3390/cancers12082320

49. Cuvellier M, Ezan F, Oliveira H et al (2021) 3D culture of HepaRG cells in GelMa and its application to bioprinting of a multicellular hepatic model. Biomaterials 269:120611. https://doi.org/10.1016/j.biomaterials.2020.120611

50. Stricker J, Falzone T, Gardel ML (2010) Mechanics of the F-actin cytoskeleton. J Biomech 43:9–14. https://doi.org/10.1016/j.jbiomech.2009.09.003

51. Hakkinen KM, Harunaga JS, Doyle AD et al (2011) Direct comparisons of the morphology, migration, cell adhesions, and actin cytoskeleton of fibroblasts in four different three-dimensional extracellular matrices. Tissue Eng Part A 17:713–724. https://doi.org/10.1089/ten.TEA.2010.0273

52. Škalamera D, Stevenson AJ, Ehmann A et al (2019) Melanoma mutations modify melanocyte dynamics in co-culture with keratinocytes or fibroblasts. J Cell Sci 132(24):jcs234716. https://doi.org/10.1242/jcs.234716

53. Papaccio F, Kovacs D, Bellei B et al (2021) Profiling cancer-associated fibroblasts in melanoma. Int J Mol Sci 22:7255. https://doi.org/10.1242/jcs.23471610.3390/ijms22147255

54. Flach EH, Rebecca VW, Herlyn M et al (2011) Fibroblasts contribute to melanoma tumor growth and drug resistance. Mol Pharm 8:2039–2049. https://doi.org/10.1021/mp200421k

55. Steer A, Cordes N, Jendrossek V et al (2019) Impact of cancer-associated fibroblast on the radiation-response of solid xenograft tumors. Front Mol Biosci 6:70. https://doi.org/10.3389/fmolb.2019.00070

56. Smalley KS, Lioni M, Herlyn M (2005) Targeting the stromal fibroblasts: a novel approach to melanoma therapy. Exp Rev Anticancer Ther 5:1069–1078. https://doi.org/10.1586/14737140.5.6.1069

57. Slominski A, Kim TK, Brożyna AA et al (2014) The role of melanogenesis in regulation of melanoma behavior: melanogenesis leads to stimulation of HIF-1α expression and HIF-dependent attendant pathways. Arch Biochem Biophys 563:79–93. https://doi.org/10.1016/j.abb.2014.06.030

58. Fang Y, Eglen RM (2017) Three-dimensional cell cultures in drug discovery and development. Slas Discov Adv Life Sci R&D 22:456–472. https://doi.org/10.1177/1087057117696795

59. Ravi M, Paramesh V, Kaviya SR et al (2015) 3D cell culture systems: advantages and applications. J Cell Physiol 230:16–26. https://doi.org/10.1002/jcp.24683

60. Ghosh S, Spagnoli GC, Martin I et al (2005) Three-dimensional culture of melanoma cells profoundly affects gene expression profile: a high density oligonucleotide array study. J Cell Physiol 204:522–531. https://doi.org/10.1002/jcp.20320

61. Lawrence MJ, Rees GD (2012) Microemulsion-based media as novel drug delivery systems. Adv Drug Deliv Rev 64:175–193. https://doi.org/10.1016/S0169-409X(00)00103-4

62. Lopes LB (2014) Overcoming the cutaneous barrier with microemulsions. Pharmaceutics 6:52–77. https://doi.org/10.3390/pharmaceutics6010052

63. Versluis AJ, van Geel PJ, Oppelaar H et al (1996) Receptor-mediated uptake of low-density lipoprotein by B16 melanoma cells in vitro and in vivo in mice. Br J Cancer 74(1996):525–532. https://doi.org/10.1038/bjc.1996.396

64. Favero GM, Paz JL, Otake AH et al (2018) Cell internalization of 7-ketocholesterol-containing nanoemulsion through LDL receptor reduces melanoma growth in vitro and in vivo: a preliminary report. Oncotarget 9:14160. https://doi.org/10.18632/oncotarget.24389